

**Characteristics and Modelling of Radiative
Boundary Discharges in ASDEX Upgrade**

R. Dux, A. Kallenbach, ASDEX Upgrade Team

IPP 10/1

February 1996



MAX-PLANCK-INSTITUT FÜR PLASMAPHYSIK

85748 GARCHING BEI MÜNCHEN

MAX-PLANCK-INSTITUT FÜR PLASMAPHYSIK
GARCHING BEI MÜNCHEN

Characteristics and Modelling of Radiative
Boundary Discharges in ASDEX Upgrade

R. Dux, A. Kallenbach, ASDEX Upgrade Team

IPP 10/1

February 1996

These are two preprints from papers submitted to PPCF.

*Die nachstehende Arbeit wurde im Rahmen des Vertrages zwischen dem
Max-Planck-Institut für Plasmaphysik und der Europäischen Atomgemeinschaft über
die Zusammenarbeit auf dem Gebiete der Plasmaphysik durchgeführt.*

Measurement and modelling of neon radiation profiles in radiating boundary discharges in ASDEX Upgrade

R. Dux, A. Kallenbach, M. Bessenrodt-Weberpals, K. Behringer, H.-S. Bosch, J.C. Fuchs, O. Gehre, F. Mast, W. Poschenrieder, H. Murmann, H. Salzmann, J. Schweinzer, W. Suttrop, ASDEX Upgrade- and NI-Team
MPI für Plasmaphysik, EURATOM Association, Garching and Berlin, Germany

February 9, 1996

Abstract

The radiation and transport characteristics of ASDEX Upgrade discharges with a neon driven radiative mantle are modelled using a 1-D radial impurity transport code that has been coupled to a simple divertor model describing particle recycling and pumping. The code is well suited to describe the measured impurity line radiation, total, soft x-ray and bremsstrahlung radiation in regions of the plasma which are not dominated by two dimensional effects. The recycling and pumping behaviour of neon as well as the bulk transport of neon for radiative boundary scenarios are discussed.

1 Introduction

Radiative cooling of the plasma boundary by controlled injection of medium Z impurities has been demonstrated to yield substantial reductions of the power flow onto the target plates as required for future reactors. The feasibility of the concept has first been shown for L-mode as well as improved I-mode on the limiter tokamak TEXTOR (SAMM *et al.*, 1993; MESSIAEN *et al.*, 1994). However, the compatibility of a radiative mantle with H-mode operation, high heating power and divertor operation was demonstrated recently on the ASDEX Upgrade divertor tokamak (GRUBER *et al.*, 1995; KALLENBACH *et al.*, 1995; NEUHAUSER *et al.*, 1995). In these experiments the radiated power fraction was feedback controlled (RAUPP *et al.*, 1995) by puffing of noble gases (mainly neon) and was tuned to such a level, that the reduced power flow across the separatrix $P^{sep} = P_{heat} - P_{rad}^{bulk}$ was just above the H→L threshold $P_{H→L}^{sep}$. By these means an H-mode with frequent small amplitude type-III ELMs accompanied by complete divertor detachment could be achieved (CDH-mode). More information about the threshold behaviour of L/H-mode transitions for radiating boundary discharges in ASDEX Upgrade is given by (KALLENBACH *et al.*, 1996).

For extrapolation of these experimental results to next step experiments a good understanding of the neon transport and the radiation characteristics is needed. The global transport properties of neon in the plasma vessel (global residence time, divertor retention) determines whether an effective feedback control of the radiated power fraction can be set up. The transport of

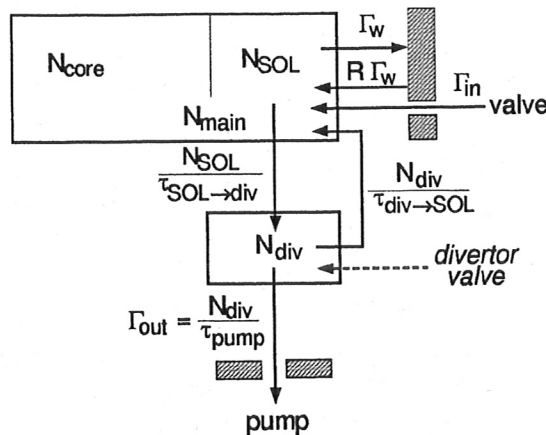


Figure 1: Sketch of the simplified recycling model used to achieve a realistic description of the neon source function for radial impurity transport calculations.

neon in the bulk plasma governs the question how much fuel dilution and impurity fraction has to be taken into account for a certain amount of radiated power. Furthermore, it is desirable to analyse the observed radiation profiles in terms of the atomic data for ionization, recombination and excitation. The exact form of the radiation profile at the plasma edge might be an important feature for defining the interaction of H-mode barrier and radiating boundary.

This paper describes in detail a simple modelling approach for the description of the neon bulk and midplane edge radiation in high power, high density radiating boundary discharges and compares the results with measured intensities of line emission, total radiation and soft x-ray emission. The quantitative comparison also includes the slow dynamic effects of the build-up and decay of the neon content on a global residence timescale, but not resolving ELMs or MHD phenomena. The global residence time results from a simple description of the neon circulation from the injection through the valve until its disappearance in the pumping system. The model focuses on the impurity transport and radiation, while the parameters of the background plasma are taken from the experiment. Modelling approaches of radiating boundary discharges, which self-consistently handle the interplay of impurity transport and radiation with heat and particle transport of the background plasma, were performed for discharges on the limiter tokamak TEXTOR (TOKAR *et al.*, 1995) and references therein and for CDH-mode discharges in ASDEX Upgrade (BECKER *et al.*, 1995).

2 Modelling of neon transport and midplane emission

The impurity transport and the midplane emission characteristics are modelled with the radial impurity transport code STRAHL (BEHRINGER, 1987). The code solves the radial continuity equation for each ionization stage of the impurity in 1-D geometry. For the transport an ansatz of anomalous diffusivities and radial drift velocities is used; a full neoclassical treatment of impurity transport can be switched on if desired.

The rate coefficients for ionization, recombination and radiation are taken from the ADAS (SUMMERS, 1994) database. For the calculation of the actual rates the code uses measured profiles of electron density and temperature in the main plasma, the scrape-off layer is treated in a simplified manner applying decay lengths which are fitted to measured data. For comparison of the atomic data set with other recently published data (CLARK *et al.*, 1995) the total cooling rate coefficient in the approximation of coronal ionization equilibrium $L(T_e)$ was calculated and

good agreement (differences are below 20 %) in the temperature range from 20 – 1000eV was found. Bremsstrahlung is calculated taking effective Gaunt factors (KARZAS and LATTEr, 1961).

An essential feature is the empirical description of recycling and pumping by a simple chamber model (KALLENBACH *et al.*, 1995). A sketch of the particle fluxes in this chamber model is given in Fig. 1. Neon is puffed into the main chamber via a calibrated valve and is distributed in the main plasma according to diffusion constants and drift velocities. At the plasma edge a fixed decay length for the impurity density is assumed and there is an according flux Γ_W towards the wall, which is assumed to recycle completely. The transport processes between scrape-off layer (SOL) and divertor chamber are treated by the ansatz of empirical loss times. Particles in the SOL are lost to the divertor with the parallel loss time constant $\tau_{SOL \rightarrow div}$. Particles in the divertor either escape to the SOL with the divertor retention time $\tau_{div \rightarrow SOL}$ or are pumped out with the pump time constant τ_{pump} .

The parallel loss time $\tau_{SOL \rightarrow div}$ can roughly be estimated from the density decay length λ and the diffusion constant D in the SOL yielding $\tau_{SOL \rightarrow div} = \lambda^2/D \approx 2.5ms$. The pump time constant $\tau_{pump} = V^{div}/S_{Ne}$ is given by the pumping speed S_{Ne} of the 14 turbomolecular pumps and an assumed effective divertor volume of $V^{div} = 3m^3$. The pumping speed for neon is a function of the neutral D_2 density in the pump duct. For low densities (molecular flow) the pumping speed for neon can be calculated from the measured pumping speed for deuterium and the ratio of the particle masses to be $S_{Ne} = 6.9m^3/s$. In the limiting case of laminar flow conditions small neon concentrations would be pumped with the same pumping speed as deuterium setting an upper limit at $S_{Ne}^{max} = 17.6m^3/s$. In the investigated parameter range a linear increase up to $S_{Ne} = 11m^3/s$ was estimated.

The determination of $\tau_{div \rightarrow SOL}$ was performed by an analysis of the observed average residence time of a neon atom in the plasma vessel. This effective particle confinement time $\tau_p^* = \tau_{pump}(1 + N^{main}/N^{div})$ depends on the relative populations in the main plasma volume N^{main} and in the divertor volume N^{div} . The ratio of the particle populations N^{main}/N^{div} is governed by the ratio of the according time constants $\tau_{SOL \rightarrow div}/\tau_{div \rightarrow SOL}$. Thus, a long divertor retention time leads to compression of neon in the divertor, which causes a small effective particle confinement time τ_p^* .

It has been shown that increased neutral flux density in the outer divertor, which is measured by ionization gauges and feedback-controlled by deuterium puffing into the main chamber, leads to a strong decrease of the effective particle confinement time τ_p^* (KALLENBACH *et al.*, 1995). In Fig. 2a the decay rate of the neon recycling flux at midplane, being approximately equal to the inverse of τ_p^* is shown versus the neutral hydrogen/deuterium flux density in the outer divertor for different isotope compositions of the plasma. These data represent attached H-modes with heating powers in the range from 4.5 to 8 MW. There is no strong isotope effect of the neon decay rate. The line gives the decay rates from the transport code, when using a fixed time constant of 2.5 ms for $\tau_{SOL \rightarrow div}$ and choosing the dependence of τ_{pump} and $\tau_{div \rightarrow SOL}$ as given in Fig. 2b. The dependence of τ_{pump} on $\Gamma_{D_2}^{div}$ was taken to be offset linearly as described above. With these values for $\tau_{SOL \rightarrow div}$ and τ_{pump} the dependence of $\tau_{div \rightarrow SOL}$ on $\Gamma_{D_2}^{div}$ could be fitted to the measured values of the effective particle confinement times. The divertor retention time $\tau_{div \rightarrow SOL}$ is found to grow with $\Gamma_{D_2}^{1.4}$. The absolute value of $\tau_{div \rightarrow SOL}$

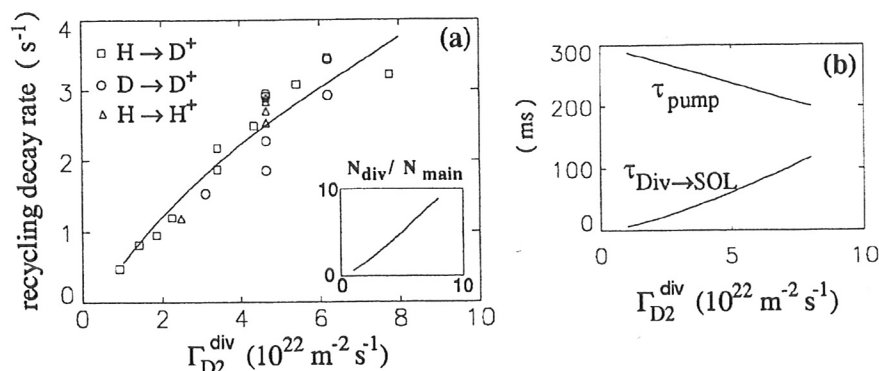


Figure 2: Recycling $1/e$ decay rates from several discharges after neon puffing and for three isotope compositions of the background plasma versus the neutral D_2 flux density in the outer divertor. The line gives the result of the transport model when using the time constants depicted in figure (b). The according ratio of neon particles in the divertor to that in the main plasma is shown in the inlay of figure (a).

depends on the absolute value of $\tau_{SOL \rightarrow div}$ and the fitting curve in Fig. 2a would be similar when decreasing both constants by 50%. This behaviour is due to the fact that the model is only sensitive to the ratio of the two time constants as long as they are small compared to the pumping time. Since the estimate of the parallel loss time is quite coarse the absolute value of the divertor retention time might be uncertain as well. However, it can experimentally be proven that the time constants can not be much larger as will be described in the next section. A more robust quantity is the compression of neon in the divertor volume. It increases with increasing decay rate and the ratio of N^{main}/N^{div} that yields the transport model is given in the insert in Fig. 2a.

3 Particle balance and puff position

In the case of small internal time constants compared to τ_{pump} the particle balance in equilibrium does not change whether the neon is puffed into the divertor or whether it is puffed into the main chamber. The particle balance is purely determined by the ratio of divertor retention time $\tau_{div \rightarrow SOL}$ and parallel loss time $\tau_{SOL \rightarrow div}$. However, if the internal time constants are of the order of τ_{pump} , the particle balance might be influenced by the puff position. Thus, discharges with identical divertor neutral flux density and different puff positions were performed to assess the magnitude of the internal time constants. The feed forward neon puff was set to a constant value in both cases and a neutral flux density of $\Gamma_{D_2}^{div} = 4.7 \cdot 10^{22} \text{ m}^{-2} \text{ s}^{-1}$ was used. The neon puff strength into the divertor was 75% of the puff strength into the main chamber.

Fig. 3 shows neon line emissions in the vacuum ultraviolet spectral range as measured at mid-plane by the SPRED spectrometer and compares it with the signals from the emission/transport calculations. The discharge with main chamber puff (# 6516) is shown in the left column and the discharge with divertor puff (# 6538) in the right column. For both discharges all time constants were taken from the global dependences of Fig. 2b: $\tau_{pump} = 242 \text{ ms}$, $\tau_{div \rightarrow SOL} = 55 \text{ ms}$, $\tau_{SOL \rightarrow div} = 2.5 \text{ ms}$. Two lines from the boron- and beryllium-like stages are shown for both dis-

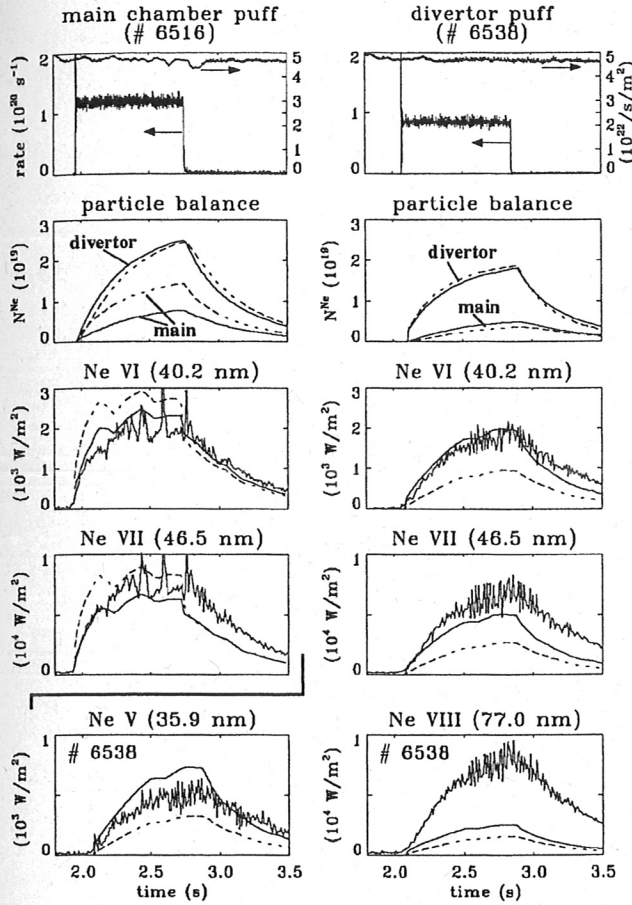


Figure 3: STRAHL modelling of the mid-plane line emission for a pair of discharges with a constant neon puff into the main chamber (# 6516) and the divertor (# 6538) in comparison to measured radiation fluxes from the SPRED spectrometer (measured at midplane with a central line-of-sight). Note that the neon puff strength into the divertor was 75% of the puff strength into the main chamber. The pictures with the neon puff also show the deuterium flux density in the divertor which was feedback controlled to the same level in both discharges. The particle balance (third row) approaches the same equilibrium distribution in both cases. The dashed lines give the result for larger internal time constants yielding the same τ_p^* .

charges and two extra lines from the carbon- and lithium-like stages are shown for # 6538 in the bottom row. The model can explain the time behaviour and the absolute size of the line emission with less than 30% deviation for the individual lines from NeV to NeVII. The NeVIII line is off by a factor of 3. All these comparisons give confidence in the simple chamber model to give a good description of the global neon transport and the neon source function. The particle balances from the transport calculation (second row) show that the majority of the neon resides in the divertor in both cases. The dashed line gives the result of the transport calculation when increasing the parallel loss time by a factor of 5, i.e. $\tau_{SOL \rightarrow div} = 12.5 \text{ ms}$. For the discharge with main chamber puff the time behaviour and the signal heights can still be fitted but to do so a large divertor retention time of $\tau_{div \rightarrow SOL} = 400 \text{ ms}$ has to be used being already a factor of ≈ 1.7 larger than the pump time constant. When using this set of time constants for the discharge with the puff into the divertor the influence of the pumps on the particle balance is already quite large and the calculated line emissions at midplane are too low by a factor of 2. This clearly demonstrates that the internal time constants are indeed small compared to the pump time constant and that the particle balance is only a function of the ratio $\tau_{SOL \rightarrow div} / \tau_{div \rightarrow SOL}$ and not of the puff position.

Similar measurements of the main chamber argon radiation versus the deuterium puff strength and the argon puff location (divertor and top of the vessel) have been performed on the DIII-D tokamak (SCHAFER *et al.*, 1995) and the interpretation given here is in line with the observations made at DIII-D. The steady state argon concentration in the main chamber varied

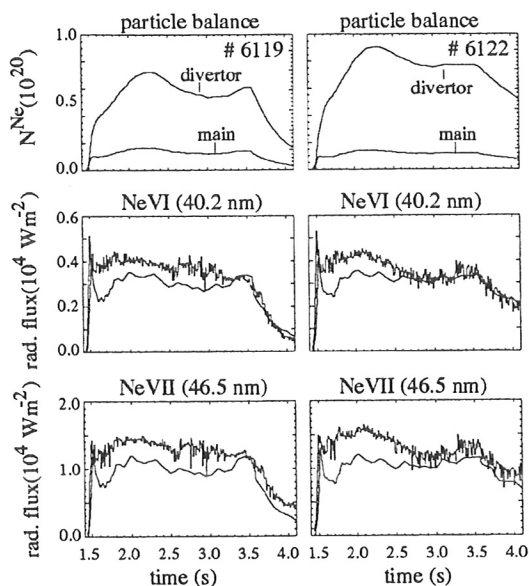


Figure 4: STRAHL modelling of the mid-plane line emission for a pair of discharges with high (# 6119) and low (# 6122) deuterium puffing and accordingly high (14 pumps) and low (4 pumps) pumping. Both discharges can be modelled with the same set of divertor retention time $\tau_{div \rightarrow SOL}$ and parallel loss time constants $\tau_{SOL \rightarrow div}$. The difference in the time behaviour only comes about by the change of τ_{pump} which is increased by 14/4 in the second case. The feedback-controlled neon puff is about a factor of 2 larger for the high puff/pump case and stops at $t = 3.5s$ in both discharges.

by a factor of 10-20 when increasing the neutral deuterium pressure in the private flux region by a factor of 6. However, a slight dependence of the main chamber concentration on the argon puff location has been found leading to the interpretation that the internal time constants of argon for the DIII-D divertor are in the range of the pump time constant.

4 Neon compression and divertor neutral flux

It has been discussed in the second section that an increase of the neutral flux density in the outer divertor produces a strong increase in divertor retention and leads to a large increase in the neon decay rate. However, at a fixed pumping speed for deuterium a certain divertor neutral flux density is always produced by the same deuterium puff rate and it cannot be decided whether the external gas puff determines the impurity flow in the scrape-off layer and the divertor retention. To answer this question a pair of discharges with equal neutral flux densities in the divertor, $\Gamma_{D_2}^{div} = 4.7 \cdot 10^{22} m^2/s$, but with largely different pumping speeds was performed. To this end all but 4 of the 14 pumps were disconnected from the torus. The neon puff was feedback controlled to reach the same amount of total radiated power (BOSCH *et al.*, 1995). The result of the transport/emission calculation is shown in Fig. 4. First the high puff case with all pumps on was modelled (# 6119). The divertor retention time and pump time constant were taken from the functions shown in Fig. 2b: $\tau_{div \rightarrow SOL} = 80 ms$ and $\tau_{pump} = 225 ms$. With these values the measured decay times of the neon line emission which were observed at midplane by the SPRED spectrometer can be fitted. The resulting particle balance from the model is shown in the first row. In the low puff case the same time constants for divertor retention and parallel loss were used as in the high puff case and only the pump time constant was multiplied by 14/4 according to the reduced pumping speed. Using the reduced neon puff rate from the experiment the decay time and the amount of neon line emission at midplane can be reproduced very nicely. Thus, the difference in the particle balance and in the decay time is only caused by the changed pumping speed. The difference in puff

strengths ($\Phi_{D_2} = 7 \cdot 10^{21} e^-/s$ for # 6119, $\Phi_{D_2} = 1.5 \cdot 10^{21} e^-/s$ for # 6122 including neutral beam injection) does not influence the retention and the particle balance, which seems to be governed by the internal flux pattern. Besides the impurity transport, no influence on the electron density and temperature profiles at the plasma edge could be observed (BOSCH *et al.*, 1995).

5 Neon transport in the bulk plasma

An important key figure for radiating boundary scenarios is the fuel dilution and central radiation loss caused by an increased central neon density (POST *et al.*, 1995). When using a transport description by anomalous diffusivity D and drift velocity v_d the radial equilibrium distribution of the neon ion density is purely determined by the dimensionless drift parameter $\alpha = v_d r / D$. Zero convection, $v_d = 0$, means constant neon density in the source-free region, constant inward drift causes a gaussian impurity profile. With the knowledge of the drift parameter the Z_{eff} increase and the increase of the central radiation can be obtained for a certain edge radiation level if the profiles of n_e and T_e are known.

For the analysis of the radiating boundary discharges the profiles of soft x-ray measurements and the time evolution of bremsstrahlung measurements in the visible range ($\lambda = 536 \text{ nm}$) have been investigated. The soft x-ray emission in the energy range above 1 keV is measured by pinhole cameras using 6 μm thick beryllium filters (BESSENRODT-WEBERPALS *et al.*, 1995) and 32 lines-of-sight from a camera that covers the whole poloidal plasma cross section have been used here. In the CDH-discharges a pronounced peaking of the soft x-ray profile develops reaching a stable level 1 s after the start of the neon injection. This peaking is accompanied by a peaking of the electron density profile (SCHWEINZER *et al.*, 1995). In Fig. 5a the measured soft x-ray radiation fluxes for each line-of-sight are drawn versus the minimal poloidal flux label of the according line-of-sight (negative flux labels for lines-of-sight below the center) for a time when the peaking reaches a stable level ($t=3 \text{ s}$). The corresponding electron density and temperature profiles are shown in Fig. 5c. The modelling results of the soft x-ray radiation fluxes are depicted for two different radial dependencies of the drift parameter. The line in Fig. 5a shows the result for a drift parameter of the form given in Fig. 5b while the broken line gives the result for zero convection demonstrating that the shape of the soft x-ray emission can only be explained when a strong inward drift is included. Without drift the soft x-ray profile is hollow since the resonance lines of the hydrogen like neon ion and partly of the helium like neon ion are above the 1 keV limit causing a maximum of the emissivity distribution around a poloidal flux label of $\rho_{pol} = 0.85$. For the case with inward drift the density of the hydrogen like neon ion at the center rises by a factor of ≈ 5 and the increased line radiation from the resonance lines together with recombination radiation and bremsstrahlung lead to the peaked soft x-ray emission. The modelling also used carbon being the main intrinsic impurity. The carbon influx was adapted to the radiation fluxes measured by the SPRED spectrometer at midplane. The same drift parameter was taken for carbon and neon. Carbon has no resonance lines above the 1 keV energy limit and only contributes to the soft x-ray radiation by the increase of bremsstrahlung. The total Z_{eff} caused by the peaked neon and carbon profile is shown in Fig. 5d while the Z_{eff} caused by carbon is given by the dashed line. In Fig. 5c the

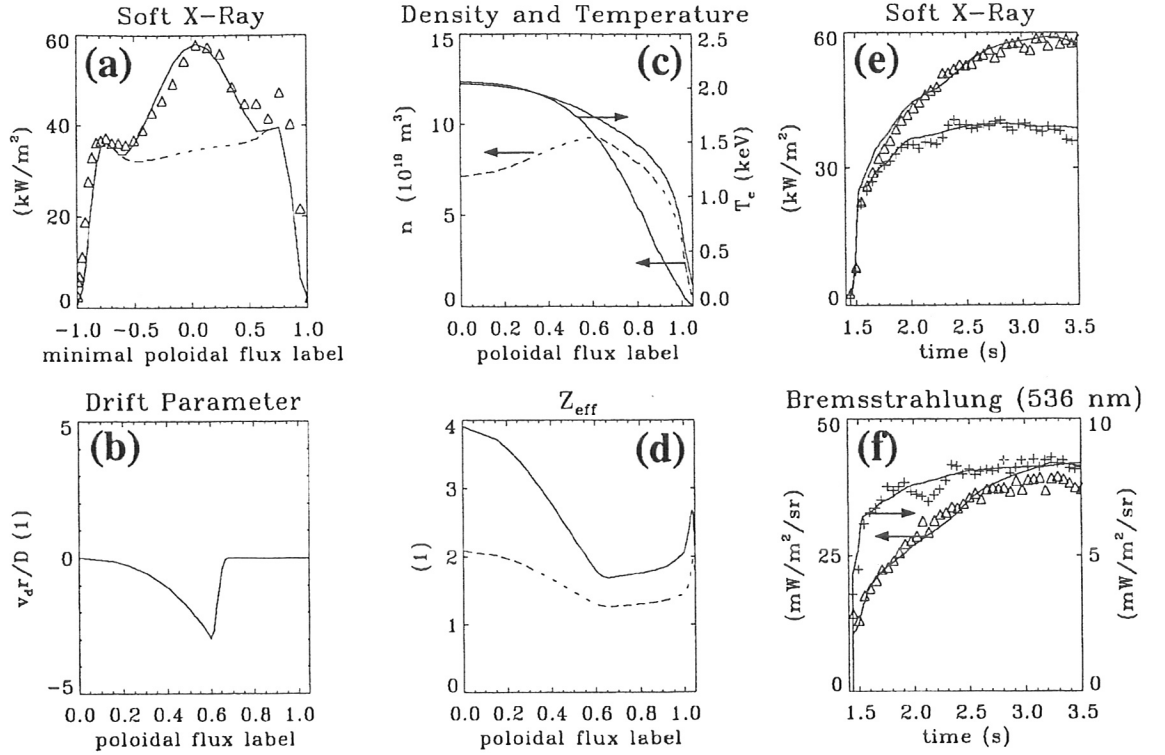


Figure 5: Comparison of soft x-ray measurements and calculated line-of-sight integrals for a stationary CDH-mode (# 6136). The peaked soft x-ray profile (a) can only be explained when using a strong inward drift (b) leading to a strongly peaked Z_{eff} shown in (d). The electron density (c) is accordingly peaked while the proton density (c, dashed line) is hollow. Measured and calculated time traces of soft x-ray radiation (e) and bremsstrahlung (f) for a central line-of-sight (triangles) and a line-of-sight tangential to $\rho_{pol} \approx 0.5$ (plus signs) demonstrate the evaluation of the peaked profile.

modelled proton density (dashed line) is shown. The proton density is hollow and the peaking of the electron density is only caused by a strongly peaked impurity density. In Fig. 5e and 5f measured and modelled soft x-ray and bremsstrahlung radiation fluxes versus time are shown for a central line-of-sight (triangles) and a line-of-sight with minimal poloidal flux label of ≈ 0.5 (plus signs). The signals of the central lines-of-sight increase up to $t \approx 2.8$ s while the more peripheral lines-of-sight very early reach a stable level. The bremsstrahlung measurements are not absolutely calibrated but their time dependence confirms the Z_{eff} development from the model.

During the development of the peaked impurity profile an $m=1$ mode with increasing amplitude is detected (NEUHAUSER *et al.*, 1995; BESSENRODT-WEBERPALS *et al.*, 1996). The mode amplitude and the peaking reach a stable level after about 1 s. No sawtooth activity can be measured. This kind of behaviour is observed for all radiating boundary discharges in the CDH-mode. When the impurity puff is too strong the plasma falls back into L-mode. In this case the sawtooth activity is not suppressed, the electron density is flat and the soft x-ray profile is hollow. These long L-phases with radiating boundary could be produced for scenarios with high H-mode threshold, i. e. $D \rightarrow D^+$ -discharges with ∇B drift away from the X-point or $H \rightarrow H^+$ -discharges, and in both cases no impurity peaking and no sawteeth suppression

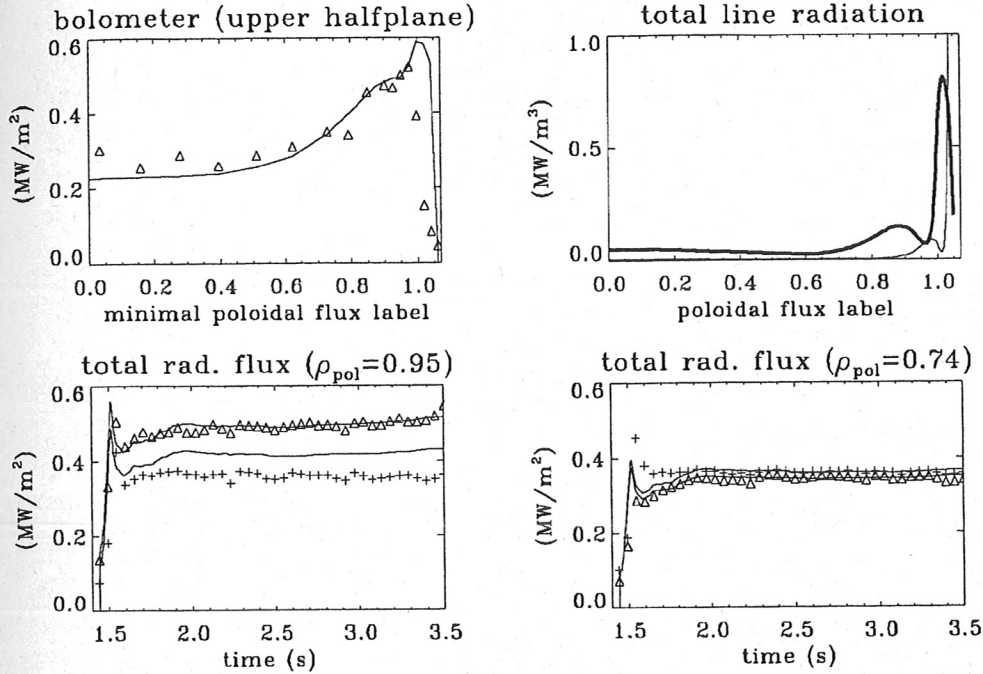


Figure 6: Comparison of bolometer measurements in the upper halfplane and calculated line-of-sight integrals for a stationary CDH-mode (# 6136). The first row gives profiles at $t=3s$ for the measured and modelled total radiation fluxes (left) and the according total line radiation emissivities (right) for neon (thick line) and carbon. The second row shows measured and modelled time traces for lines-of-sight with different minimal poloidal flux label for two bolometer cameras.

are observed. When the impurity puff is not strong enough to cause a transition from the H-mode to the CDH-mode, that means an H-mode with high boundary radiation and type-I ELMs with reduced frequency, the electron density is again flat, the soft x-ray profile is hollow and sawteeth are observed. Up to now it cannot be decided whether the impurity peaking causes the suppression of the sawteeth or, whether the lack of sawteeth causes the impurities to peak.

6 Emissivity profiles in the upper halfplane

The total emission profile for the CDH-discharge of the last section (# 6136) was calculated from the same modelling results as which were used to figure out the soft x-ray and bremsstrahlung signals. Fig. 6 shows the comparison of the resulting line-of-sight integrals for the total radiation and the bolometer measurements for the same time point as in Fig. 5 ($t=3s$). The x-axis gives the minimal poloidal flux labels of the according lines-of-sight, which belong to a camera observing the upper half of the plasma from the outer midplane. The total emissivity is dominated by the line radiation and the underlying line emissivity profiles for neon (upper line) and carbon (lower line) are shown in the upper right picture indicating the minor effect of carbon in this case. Finally measured and modelled time traces for lines-of-sight with different minimal poloidal flux labels are given. Each of these pictures contains a line-of-sight from a camera situated at midplane (triangles) and from a camera situated 1 m above the

midplane on the outer side of the torus (plus signs). Inside the separatrix the total radiation profile is very nicely described by the model. Outside the separatrix the model delivers too high values mainly due to the carbon line radiation. This is due to the one-dimensional nature of the model, which cannot describe the spatial variations of the carbon influx from the inner heatshield to the upper outer side of the torus.

7 Conclusions

A simple chamber model for recycling and pumping of neon is used and found well suited to describe the neon source function at midplane. The divertor retention time $\tau_{div \rightarrow SOL}$ depends only on the divertor neutral flux density and is in the range of 50-100 ms for high neutral flux densities. Since $\tau_{div \rightarrow SOL}$ is small compared to τ_{pump} the particle balance between main chamber and divertor cannot be significantly influenced by the puff position. The neon transport in the bulk sensitively depends on the confinement mode. In H-mode with type-I ELMs as well as in L-mode no peaking of neon can be observed. In CDH-mode, however, there is a strong inward drift and a peaking of neon occurs which finally reaches a stable level. As long as sawteeth activity is observed (H-, L-mode) the impurity profiles are flat, while the CDH-mode has no sawteeth and exhibits impurity peaking. Inside the separatrix the total emission profiles in the upper halfplane can be modelled by the radial impurity transport model.

References

- BECKER, G., FAHRBACH, H., GEHRE, O., GERNHARDT, J., KALLENBACH, A., SCHWEINZER, J., THE ASDEX UPGRADE TEAM, and NI-TEAM (1995). in *Controlled Fusion and Plasma Physics, Proc. 22nd European Conference, Bournemouth, 1995, European Physical Society, Geneva, Vol. 19 C, Part I*, 25-28.
- BEHRINGER, K. (1987). 'Description of the impurity transport code STRAHL', JET-R(87)08, JET Joint Undertaking, Culham.
- BESSENRODT-WEBERPALS, M., DE BLANK, H. J., MARASCHEK, M., et al. (1996). submitted to *Plasma Physics and Controlled Fusion*.
- BESSENRODT-WEBERPALS, M., FUCHS, J. C., SOKOLL, M., and THE ASDEX UPGRADE TEAM (1995). 'Soft X-Ray Diagnostics for ASDEX Upgrade', Rep. IPP 1/290, Max Planck Institut für Plasmaphysik, Garching.
- BOSCH, H.-S., DUX, R., HAAS, G., KALLENBACH, A., et al. (1995). submitted to *Physical Review Letters*.
- CLARK, R. E. H., ABDALLAH, J., and POST, D. (1995). *Journal of Nuclear Materials* **220-222**, 1028-1032.
- GRUBER, O., KALLENBACH, A., KAUFMANN, M., et al. (1995). *Phys. Rev. Lett.* **74**, 4217-4220.

- KALLENBACH, A., DUX, R., BOSCH, H.-S., *et al.* (1996). *submitted to Plasma Physics and Controlled Fusion*.
- KALLENBACH, A., DUX, R., MERTENS, V., *et al.* (1995). *Nucl. Fusion* **35**, 1231-1246.
- KARZAS, W. J. and LATTER, R. (1961). *Astrophysical Journal Supplements* **VI**, 167-212.
- MESSIAEN, A. M., ONGENA, J., SAMM, U., *et al.* (1994). *Nucl. Fusion* **34**, 825-836.
- NEUHAUSER, J. *et al.* (1995). *Plasma Phys. Controlled Fusion*, A37-A51.
- POST, D., ABDALLAH, J., CLARK, R. E. H., and PUTVINSKAYA, N. (1995). *Phys. Plasmas* **2**, 2328-2336.
- RAUPP, G., GRUBER, O., KALLENBACH, A., MERTENS, V., NEU, G., TREUTTERER, W., ZEHETBAUER, T., ZASCHE, D., and THE ASDEX UPGRADE TEAM (1995). 'Discharge Supervision Control on ASDEX Upgrade', *submitted to Fusion Technology*.
- SAMM, U., BERTSCHINGER, G., BOGEN, P., HEY, J. D., HINTZ, E., KÖNEN, L., LIE, Y. T., POSPIESZCZYK, A., SCHORN, R. P., SCHWEER, B., TOKAR, M., and UNTERBERG, B. (1993). *Plasma Phys. Controlled Fusion* **35**, B167-B175.
- SCHAFFER, M. J., WHITE, D. G., BROOKS, N. H., CUTHBERTSON, J. W., KIM, J., LIPPMANN, S. I., MAHDAVI, M. A., MAINGI, R., and WOOD, R. D. (1995). *Nucl. Fusion* **35**, 1000-1007.
- SCHWEINZER, J., FIEDLER, S., *et al.* (1995). *in Controlled Fusion and Plasma Physics, Proc. 22nd European Conference, Bournemouth, 1995, European Physical Society, Geneva, Vol. 19 C, Part III*, 253-256.
- SUMMERS, H. P. (1994). 'Atomic data and Analysis Structure', *JET-IR 06, JET Joint Undertaking, Abingdon*.
- TOKAR, M. Z., BAELEMANS, T., PHILIPPS, V., REITER, D., SAMM, U., UNTERBERG, B., *et al.* (1995). *Plasma Phys. Controlled Fusion* **37**, A241-A253.

Characteristics of radiative boundary discharges with different impurity injection conditions

A. Kallenbach, R. Dux, H.-S. Bosch, K. Büchl, J. C. Fuchs, O. Gehre, G. Haas, A. Herrmann, W. Herrmann, W. Junker, M. Kaufmann, V. Mertens, F. Mast, J. Neuhauser, S. de Peña Hempel, F. Ryter, J. Schweinzer, K.-H. Steuer, W. Suttrop, H. Zohm, ASDEX Upgrade- NI- and ICRH-Teams
MPI für Plasmaphysik, EURATOM Association, Garching & Berlin, Germany

February 8, 1996

Abstract

Operational parameters of highly radiative divertor discharges in the ASDEX-Upgrade tokamak are investigated for different confinement modes and radiating species. The net heat flow across the separatrix, P_{sep} , is determined using bolometric radiation profiles for steady state conditions as well as during H \rightarrow L and L \rightarrow H transitions. The radiation-corrected L \rightarrow H threshold is not affected by gas puffing and is described by $P_{sep}^{L\rightarrow H} = 0.125 \cdot \bar{n}_e \cdot B_t \cdot (2/A_{plasma}) [MW, 10^{19} m^{-3}, T, amu]$. The H \rightarrow L threshold power, which is typically lower by a factor of two without strong deuterium puffing, is increased by heavy gas puffing leading to $P_{sep}^{H\rightarrow L} \approx P_{sep}^{L\rightarrow H}$. In the vicinity of the radiation-induced H \rightarrow L transition, a general alignment of H and L mode is observed with regard to global energy confinement time and edge density and temperature profiles. The H \rightarrow L transition itself exhibits a smooth evolution in time. Reduction of target plate power load down to only 10 % of the total heating power is easily achieved by edge radiation in the CDH-mode for low $P_{thres}^{H\rightarrow L}$ conditions. However, this reduction is attributed mainly to radiation from inside the separatrix and is connected to relatively high values of the core Z_{eff} . These results emphasize the importance of the development of more closed divertor concepts, leading to higher divertor radiation levels and lower core Z_{eff} .

1 Introduction

Although impurity-induced, improved L-modes exhibit quite high energy confinement (SAMM *et al.*, 1993) (NEUHAUSER *et al.*, 1995), the H-mode is still the prime candidate for the reactor operational regime (ITER-JCT AND HOME TEAMS, 1995) owing to the narrow confinement margin for the achievement of ignition and self-sustained burn. Therefore, indispensable measures to reduce the power load of the divertor have to be compatible with H-mode operation. On the other hand, the intense power bursts connected with type-I ELM activity in the H-mode may not be acceptable in a reactor.

The Completely Detached High-Confinement (CDH-) mode recently discovered in ASDEX Upgrade (GRUBER *et al.*, 1995) would meet the requirements for an operational mode of a reactor as far as target power load is concerned: Radiative power removal closely inside the separatrix moderates the ELM activity from type-I to type-III enabling the divertor plasma to buffer the remaining small power bursts before reaching the target plates, while high H-mode energy confinement is preserved. However, the extrapolability of this regime to reactor conditions mainly depends on the relative locations of the H→L and detachment power thresholds: The CDH mode in ASDEX Upgrade is obtained only in deuterium plasmas, where the H→L power threshold is low and subsequent detachment relatively easy to achieve (BOSCH *et al.*, 1996b). Another major point of concern are the relatively high values of Z_{eff} connected with radiative scenarios exhibiting full detachment. Since neither the H-mode- nor the detachment threshold in a reactor are precisely known so far, flexibility has to be demonstrated in present day experiments in order to develop different solutions which can meet the various requirements.

This study investigates and compares the behaviour of neutral beam heated divertor discharges with strong edge radiation caused by controlled puffing of neon, nitrogen and argon. Special emphasis is placed on experimental conditions in the vicinity of the radiation-induced H→L transition. Chapter 2 gives a short review on the influence of the divertor neutral deuterium flux on the behaviour of discharges with impurity injection. A comparison of the behaviour of highly radiative discharges with neon, argon and nitrogen injection is presented in Chapter 3. Chapter 4 deals with the L-H threshold behaviour in radiative scenarios. Operational diagrams of radiative H-modes are presented in Chapter 5, while aspects of plasma contamination and Z_{eff} during strong radiation are discussed in Chapter 6.

2 Experimental conditions and influence of the divertor neutral flux

An important experimental parameter for radiative scenarios appears to be the neutral deuterium flux in the divertor. It is measured by ionization gauges and feedback-controlled by deuterium puffing in the main chamber. An increasing divertor neutral density has two beneficial effects on the performance of discharges with impurity injection (KALLENBACH *et al.*, 1995): Firstly, the divertor retention increases leading to better pumping of noble gases and faster feedback response on the request of radiation reduction. Secondly, the higher divertor neutral density is connected with a higher edge electron density in the main plasma (NEUHAUSER *et al.*, 1995) and increased ELM activity. These effects lead to a higher radiative capability at the edge and core screening of impurities. The price for the improved radiative behaviour is a moderate degradation of the energy confinement of roughly $\tau_E \propto n_{0,div}^{-0.1}$. Although contraproductive to the achievement of very high energy confinement (ALLEN *et al.*, 1995), a high neutral deuterium flux may be inevitable for the achievement of good helium divertor compression and pumping in a reactor anyway: Similar to the behaviour observed for neon, the helium pumping was found to increase strongly with the deuterium neutral flux in the divertor (HAAS *et al.*, 1995). Corresponding experiments with simultaneous reduction of pumping speed and deuterium puff-rate have shown, that the divertor impurity retention is determined by strong internal deuterium fluxes. Variation of the net deuterium flux from the main chamber to the pumps in the divertor up to $7 \cdot 10^{21}$ atoms/s revealed no variation in confinement, profile shapes, impurity compression and radiation, while the neutral D₂ flux level in the divertor was kept constant (BOSCH *et al.*, 1996a). Another consequence of the dominance of internal fluxes is the unimportance of the puff location (main chamber or divertor) for the steady-state radiation distribution as long as the divertor retention time is considerably shorter than the pumping time (DUX *et al.*, 1996).

For the experiments of this paper, neutral beam heating is started after the plasma current has reached its flattop value. Next, the divertor neutral gas feedback is activated and finally the radiation feedback system is enabled. The discharges are terminated with the reversed sequence, allowing for about 0.5 s with high neutral divertor flux to improve removal of the seed gas and full heating power to avoid a H→L backtransition with subsequent density limit disruption. Details of the experimental procedure and feedback control for radiative scenarios in ASDEX Upgrade have been published elsewhere (KALLENBACH *et al.*, 1995).

3 Comparison of highly radiating discharges with Ne, Ar and N₂ injection

Fig. 1 shows a comparison of 3 discharges with high radiation levels obtained by injection of Ne, Ar and N₂ under otherwise almost identical external parameters. Discharge # 6136 exhibits

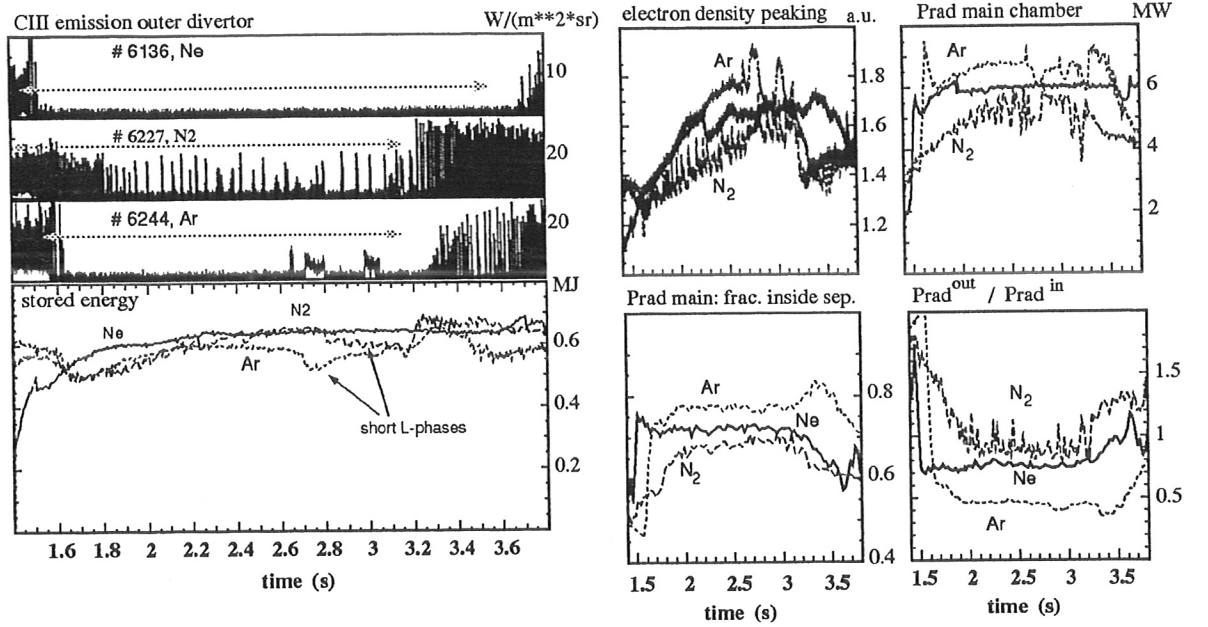


Figure 1: Comparison of highly radiating discharges with Ne, Ar and N₂ injection in the main chamber. $\bar{Z}_{eff}^{<0.5} \approx 3$ in the H-mode at $t = 2.5$ s for all 3 discharges. $P_{heat} = 7.5$ MW, $D^0 \rightarrow D^+$ NBI, $I_p = 1$ MA, $q_{95} = 4$.

the CDH-mode with quasi steady-state stored energy, radiation level (feedback-controlled) and density peaking. Using argon, the electron density profile shows higher peaking factors and short L-phases are triggered by the high radiation level. With nitrogen, compound-ELMs (ZOHM *et al.*, 1995) and short L-phases appear at a radiation level lower than that obtained with neon. Strong wall pumping of nitrogen is usually observed during experiments with N₂ puffing, making feedback control easier. On the other hand, the formation of a high nitrogen wall inventory makes its use as a seed element for continuously operating devices questionable. The fraction of main chamber radiation emitted inside the separatrix, f_{in} , which is important for the H-mode behaviour is calculated with a fitting procedure to bolometer line integrals in the upper halfplane under the assumption of constant emissivity on flux surfaces $E = f(\rho_{pol})$ with a prescribed functional profile shape. Two Lorentzian half-profiles were chosen to allow for a parametrization of E , whose decay lengths, peak intensity and position were varied in a least-squares fitting procedure to reproduce the measured radiation line integrals. For typical conditions, the emission maximum was localized just at the separatrix, with a steeper decay

to the outside than to the inside. The obtained emission function $E = f(\rho_{pol})$ is then used to derive the total radiation inside the separatrix, $P_{rad}^{in} = f_{in} \cdot P_{rad}^{main}$, using the total main chamber radiation taken from 30 line integrals of the horizontal bolometer camera above the X-point. $P_{rad}^{out} = (1 - f_{in}) \cdot P_{rad}^{main} + P_{rad}^{div}$, the total radiation outside the separatrix, is the sum of the SOL radiation in the main chamber and the divertor radiation, the latter taken from the deconvolution of all the 72 bolometer line integrals (FUCHS *et al.*, 1994). The procedure described above is the attempt to take into account the contribution of the X-point radiation to P_{rad}^{in} , since the full deconvolution procedure is not capable to evaluate the radiation distribution around the X-point with enough spatial resolution to separate contributions from inside and outside the separatrix owing to the limited number of viewing chords.

As shown in Fig. 1 the total plasma emissivity is shifted towards the interior (i.e., higher temperatures) with increasing Z of the radiating species, as one would expect from simple radiative loss rate considerations (POST *et al.*, 1995) and from analytical modelling including transport effects (TOKAR, 1994). Simultaneously with the rising radiation level inside the separatrix, SOL and divertor radiation decrease leading to a reduction of the parameter $P_{rad}^{out}/P_{rad}^{in}$ by a factor of 2 from nitrogen to argon. While this parameter shows the best (i.e. highest) values with nitrogen, the occurrence of large compound ELMs which lead to high peak power loads of the target (see also Chapter 4.3) plate remain a disturbing feature probably not suitable for operation conditions of a reactor.

4 L/H-mode transitions and threshold behaviour

An important parameter for radiative H-mode scenarios is the value of the H→L threshold power. It mainly depends on the toroidal magnetic field, the electron density and in a not well-established manner on the edge recycling level. For typical plasma conditions without additional central radiators, the separatrix power flux is often treated synonymously with the heating power. Taking intrinsic central radiation into account (typically 25 % of the heating power for deuterium plasma and about 15 % for hydrogen),

$$P_{sep}^{L \rightarrow H} = P_{heat} - P_{rad}^{in} = 0.125 \cdot \bar{n}_e \cdot B_t \cdot (2/A_{plasma}) [MW, 10^{19} m^{-3}, T, amu] \quad (1)$$

is a good approximation for 'standard' conditions (i. e. no strong gas puffing, no additional impurities) on ASDEX Upgrade, the corresponding value for the H→L transition being about a factor of 2 lower, known as the H-mode hysteresis (RYTER *et al.*, 1994b). The plasma surface is about 44 m². Without additional impurity radiation and strong deuterium puffing,

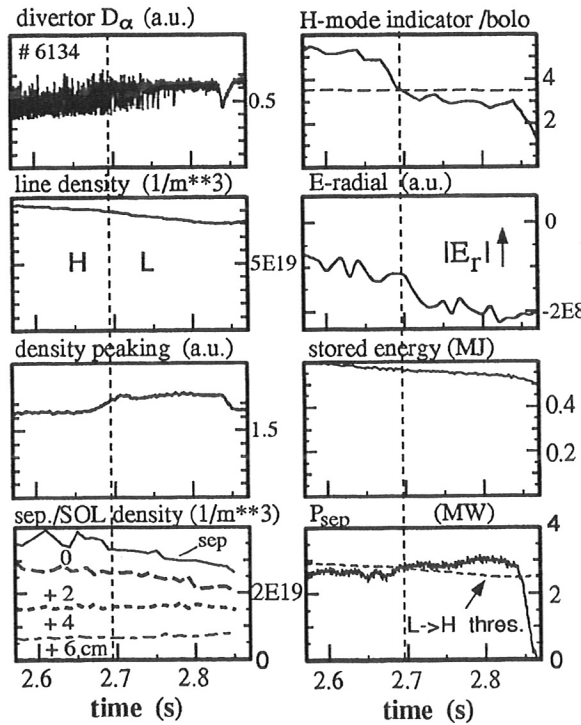


Figure 2: Time traces for a discharge with strong neon puffing leading to a transition from the CDH- to L-mode. Divertor D_α -emission, line-averaged density, electron density peaking factor derived from two interferometer line integrals, midplane separatrix and SOL electron densities from lithium beam diagnostics, H-mode indicator signal from bolometry, measure of radial E-field from CX particle analysis, stored energy from magnetic equilibrium and power flux through the separatrix calculated from heating power and deconvolution of bolometer measurements. The vertical line indicates the assumed time of the H→L transition. The discharge disrupted after Marfe formation at $t=2.9$ s. $D^0 \rightarrow D^+$ NBI, $P_{heat} \approx \text{const} = 7.5$ MW, $I_p = 1$ MA, $q_{95} = 4$, $\Gamma_{D_2}^{div} = 3.3 \cdot 10^{22} m^{-2} s^{-1}$.

the transitions between L- and H-mode occur only at rather low heating powers and plasma energy contents. For these conditions, also a clear difference between L- and H-mode energy confinement times is observed.

4.1 H→L transition due to impurity radiation

The H-mode behaviour changes considerably, when higher heating powers are applied in combination with impurity injection. These conditions produce a rather energetic plasma core, but a considerable fraction of the power flux is lost by radiation before being conducted across the separatrix. For these experimental conditions, the otherwise pronounced difference in energy confinement between L- and H-mode becomes weak, as can be seen in Fig. 1. Beyond this

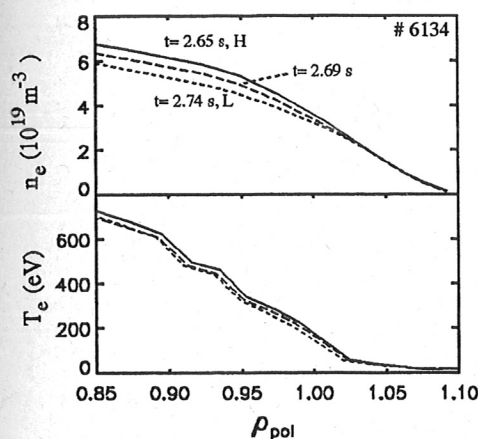


Figure 3: Edge electron temperature and density profiles measured by ECE and Lithium beam diagnostics near the outer midplane. Profiles are given prior to, around and short after the H→L transition shown in Fig. 2.

observation, inspection of a number of impurity-induced H→L transitions shows that even the definition of the H-mode is going to become ambiguous. This is demonstrated in Fig. 2, where various time-traces are shown for a discharge which was forced back to L-mode by strong neon puffing. The 'standard indicators' for the discharge state, divertor D_α emission, energy content and line-averaged density exhibit a continuous and smooth transition evolving over several hundred milliseconds with no visible jump or steepening. The degradation of energy confinement and particle content is accompanied by the appearance of $m=1, n=1$ mode activity. During the temporal evolution from 'pure H' to 'pure L' state, the type-III ELMs seen on the D_α signal change into dithering L-H transitions and further on to negative 'H-spikes' emanating from an increased L-mode level. Pronounced transitions are only detected on the peaking factor of the density profile and on a specific indicator signal constructed from bolometer measurements further explained in Fig. 4. Edge profiles of electron temperature and density just before, during and after the H→L transition are shown in Fig. 3. While almost no change is seen in the temperature profile, the density decreases around and inside the separatrix. The reduction of the density causes a partial re-attachment of the outer divertor leading to an increase of the divertor radiation. This radiation is measured routinely and is therefore a well suited monitor signal to determine whether a highly radiating discharge is in H- or L-mode. Such information will be highly valuable for online discharge control systems, e.g. to reduce the neon puff rate after a transition to L-mode is detected (RAUPP *et al.*, 1995).

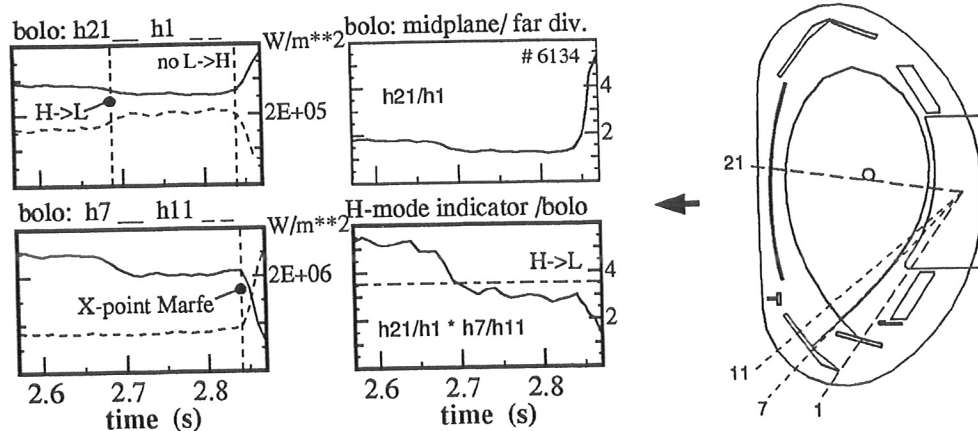


Figure 4: Indicator signal to distinguish between radiating H-mode and L-mode constructed from line integrals of the 'horizontal' bolometer camera. The arrangement of the used lines of sight with respect to the separatrix position is indicated on the right-hand-side. The bolometer line h1 probes radiation in the outer divertor outside the strike point and is a measure for the power flux in the divertor. The midplane chord h21 acts as a coarse normalization for different heating powers and impurity concentrations. The chord ratio h7/11 indicates the occurrence of an X-point Marfe shifting the radiation pattern near the X-point upward. Since this Marfe activity is coupled to a strong reduction of the power flux to the divertor, the h1 emission decreases considerably. Therefore multiplication of h21/h1 with h7/h11 results in an indicator signal which is robust against misinterpretation of the L-mode with X-point Marfe as H-mode.

The determination of the transition time is confirmed by an indirect measurement of the radial electric field derived from charge exchange particle analysis: The gradient of the slowing-down spectrum of ripple-trapped beam ions is a sensitive measure of the radial electric field near the separatrix (HERRMANN and THE ASDEX UPGRADE TEAM, 1995). Despite the effort to fix the transition time using all available diagnostics, its assignment is still uncertain within about ± 10 ms because it is not a sharp event.

4.2 L-H-L hysteresis

Without additional gas puffing, the H \rightarrow L transition generally occurs at a lower power than the L \rightarrow H transition. This 'H-mode hysteresis' amounts to about a factor of 2 with the ion- ∇B drift towards the X-point ('favourable' drift direction). With the ∇B drift away from the X-point, the L \rightarrow H threshold is about a factor of 2 higher, while the H \rightarrow L threshold is similar for both drift directions, leading to an even higher hysteresis with $\nabla B \leftarrow X$ (RYTER *et al.*, 1994a).

Figs. 5 and 6 compare the power flux into the separatrix derived from heating power and bolometer measurements with the prediction for $P_{sep}^{L \rightarrow H}$ according to Eq. 1. Allowing for some

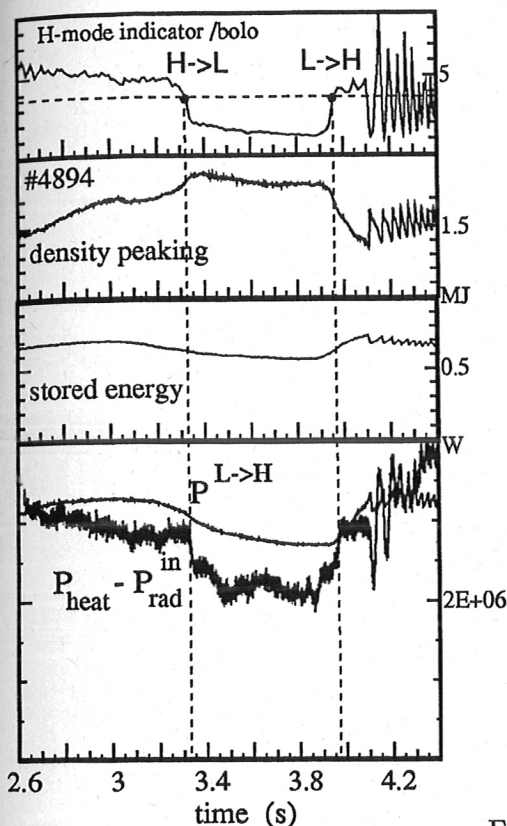


Figure 5: Time traces for a discharge with $H \rightarrow L$ and $L \rightarrow H$ transitions by neon puffing. $D^0 \rightarrow D^+$ NBI, $P_{heat} = 7.5$ MW, $I_p = 1$ MA, $q_{95} = 4$.

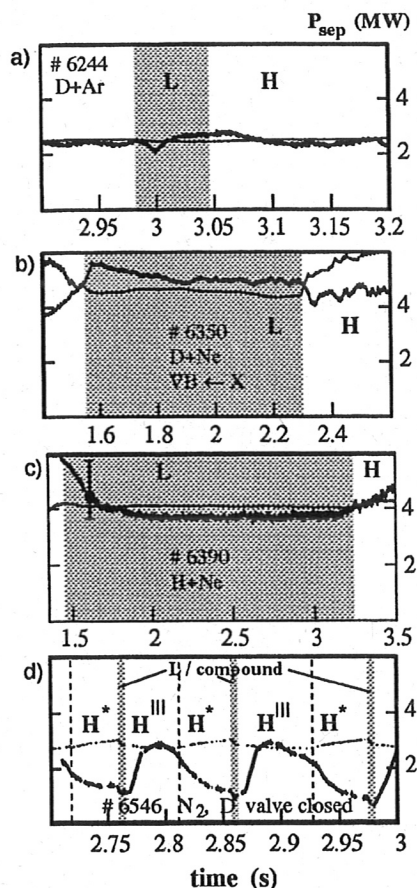


Figure 6: $H \rightarrow L$ and $L \rightarrow H$ threshold behaviour for low (D plasma, ion ∇B drift $\rightarrow X$) and high (H plasma or ion ∇B drift $\leftarrow X$) threshold conditions. solid curve: measured P_{sep} , thin curve: $P_{sep}^{L \rightarrow H}$ predicted by Eq. 1. $D^0 \rightarrow D^+$ or $H^0 \rightarrow H^+$ NBI, $I_p = 1$ MA, $q_{95} = 4$ $P_{heat} = 7.5$ MW, d) 5.5 MW.

uncertainty in P_{rad}^{in} due to the bolometer deconvolution procedure, the result is as following: The usually low $H \rightarrow L$ threshold increases in gas puff/radiative scenarios up to the value of the $L \rightarrow H$ threshold, which is little or not affected: The L-H-L hysteresis is lost. This behaviour is also observed for conditions with increased $L \rightarrow H$ power threshold, namely for hydrogen discharges (Fig. 6b) and discharges with the ion ∇B drift away from the X-point (Fig. 6c). The question arises whether the gas puff or the radiative boundary is the origin of the loss of hysteresis. Overlooking some weaknesses of the current experimental database, the deuterium gas flux, either due to direct puffing or to backstreaming from the divertor under high neutral pressure conditions, seems to be responsible for the destruction of the L-H-L hysteresis: A rise in the $H \rightarrow L$ threshold power flux is also observed in discharges with strong hydrogen puffing

injection and power flow P_{sep} close to the $P^{L \rightarrow H}$ threshold predicted by Eq 1. The neutral flux level in the divertor is continuously increased by hydrogen puffing in the main plasma. Except for a slight decrease of the stored energy, all bulk plasma parameters remain constant, including the line-averaged density and the density profile shape. The electron density in the SOL, however, increases with the divertor neutral recycling level. The $H \rightarrow L$ transition observed at $t = 2.25$ s shows an ELM behaviour similar to the radiation-induced transition shown in Fig. 2. Since \bar{n}_e , P_{rad} and B_t are constant over the transition, the most obvious explanation of the $H \rightarrow L$ transition is the increase of the $H \rightarrow L$ threshold by the increasing (internal) neutral flux. It should be noted, that there is also evidence from theory for the existence of a critical neutral density above H-mode bifurcation cannot occur (SHAING and HSU, 1995). The time evolution of several shots with different gas puffing rates indicates that the gas puffing itself is not the cause of the threshold change. The assumption, that the high neutral hydrogen/deuterium flux

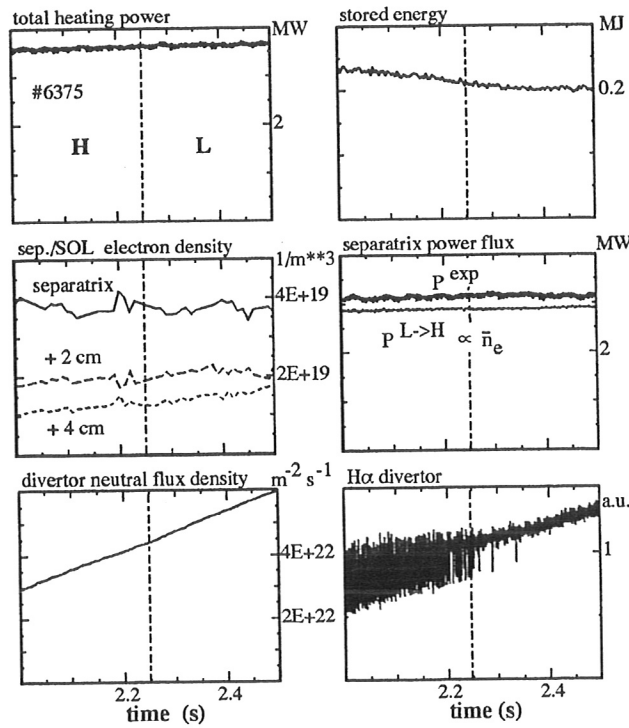


Figure 7: Time traces for a discharge with a $H \rightarrow L$ transition due to increasing hydrogen recycling level. $I_p = 0.8$ MA, $q_{95} = 3.8$

level and not the radiation is responsible for the loss of hysteresis is further supported by Fig. 6d showing P_{sep} and P_{sep}^{L-H} from Eq. 1 from a discharge with strong nitrogen radiation and low deuterium recycling level (nitrogen enters the main plasma via puffing into the divertor, D_2 valves are closed). Quiescent H-modes (H^*) occur under these conditions, which are terminated by a strong compound ELM at $P_{sep} = P_{sep}^{L-H, standard} / 2 \approx P_{sep}^{H-L, standard}$ and therefore exhibit the 'normal' L-H-L hysteresis. With high neutral deuterium flux, such quiescent H-modes have not

been observed in radiative discharges. This is probably a result of the lack of hysteresis, since the density increase during the H^* phase in the vicinity of P_{sep}^{H-L} rapidly triggers an intense compound ELM.

4.3 ELM activity

The occurrence of edge localized modes (ELMs) is an inevitable ingredient of steady-state H-mode operation. Typical time traces of ELM activity in the light of CIII emission above the outer divertor plate are illustrated in Fig. 8. The CIII emission is usually a convenient measure

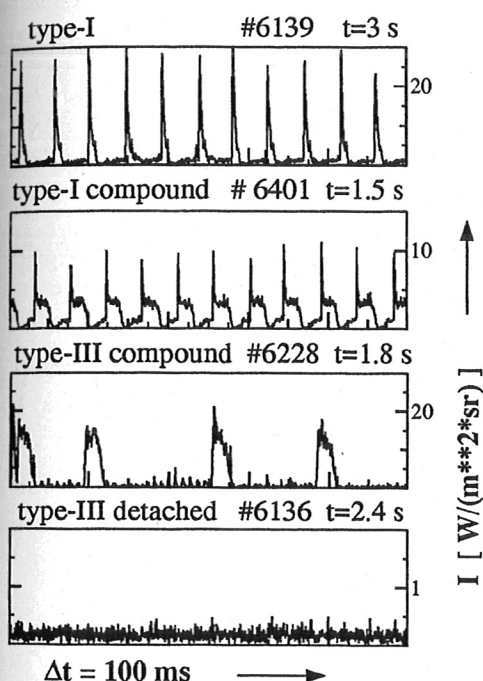


Figure 8: Various types of ELM activity in the light of CIII emission ($\lambda = 465$ nm) integrated along a radial viewing line closely above the outer target plate.

for the power flux to the target plate and exhibits lower noise and higher temporal resolution in comparison to our thermography diagnostic. Pure type I and type III ELM activities (DOYLE *et al.*, 1991) are easily separated by their frequency range of the order of 100 Hz and 1-2 kHz, respectively. In the vicinity of the threshold separatrix power flux, P_{sep}^{L-H} , compound ELMs occur, which lead to higher power load of the divertor plate. They consist of regular ELMs (type I or type III) which trigger a short L-phase of a few msec duration. Compound ELMs during completely detached type III (CDH-) ELMs usually transiently re-attach to the target plate. Compound ELMs in ASDEX Upgrade are much more frequently observed in hydrogen than in deuterium plasmas, and could not be avoided with nitrogen as seed element so far. The strongest compound ELMs are those terminating longer lasting quiescent H^* phases.

The question of tolerable ELM-types for a reactor is still open. CDH-ELMs would be fine, if necessary purity and confinement criteria could be met. Moderately attached type III ELMs

are perhaps tolerable, while the possible occurrence of type-I or strong compound ELMs is not acceptable. Unfortunately, best confinement performance is achieved under condition of very low neutral recycling levels in the main chamber, which implies to a certain degree the lack of a buffering high neutral gas pressure in the divertor.

5 Radiative H-mode operational region

Figure 9 shows P_{sep} versus $\bar{n}_e \cdot B_t$ for discharges with various radiation levels. The dashed line indicates the 'standard' L→H threshold corrected for intrinsic radiation following Eq. 1 and including the isotope effect via the factor $(2/A_{plasma})$. The data points represent measurements time-averaged over an appropriate time interval (typ. 20-200 ms) in order to reduce statistical errors and to achieve proper averaging with respect to ELMs. Different H- and L-mode types are distinguished by symbols.

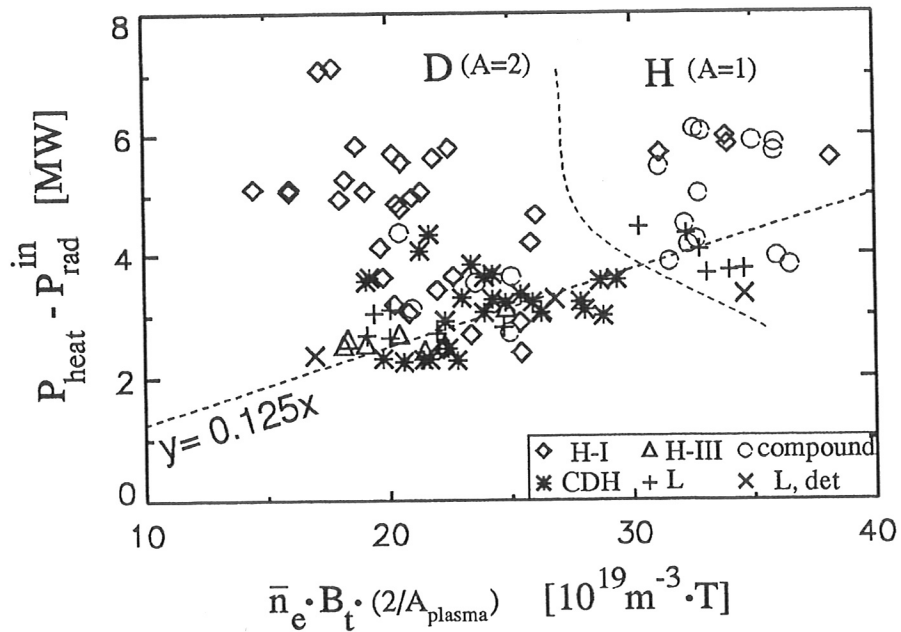


Figure 9: Operational diagram of radiative discharges with respect to the standard L→H transition threshold for D and H plasmas. Ne, Ar and N₂ injection, $P_{heat} = 5-8$ MW, $I_p = 0.8-1$ MA, $q_{95} = 2.8-4$.

The H-mode threshold according to Eq. 1 and the assumption of the absence of the L-H-L hysteresis in these scenarios gives a proper description of the operational space of radiative scenarios. It is important to note that no (L and H) data points exist far below the dashed L-H threshold line in Fig. 9, i. e. P_{sep}^{L-H} is near the lowest value of P_{sep} compatible with stable

operation. The CDH-mode data points of Fig. 9 correspond to electron densities ranging from 65 to 90 % of the Greenwald limit.

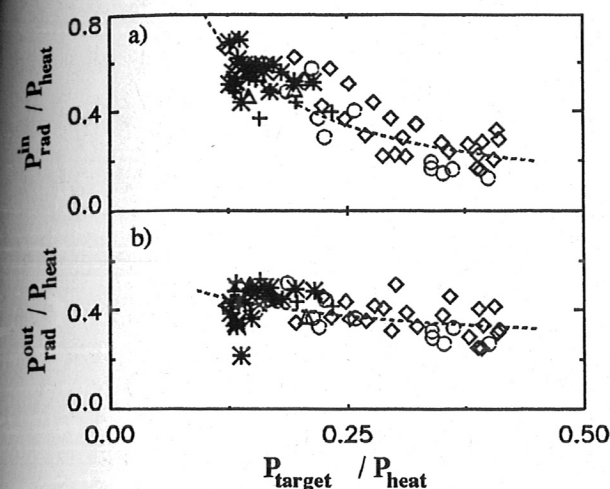


Figure 10: a) Radiation inside and b) radiation outside (SOL+divertor) the separatrix versus the sum of the power loads of the inner and outer divertor from thermography; all quantities normalized to the total heating power. Discharges of the database shown in Fig. 9, $P_{heat} = 5-10$ MW, $\bar{P}_{heat} = 7.1$ MW. The dashed curves represent (simple) power-law fits to the data points.

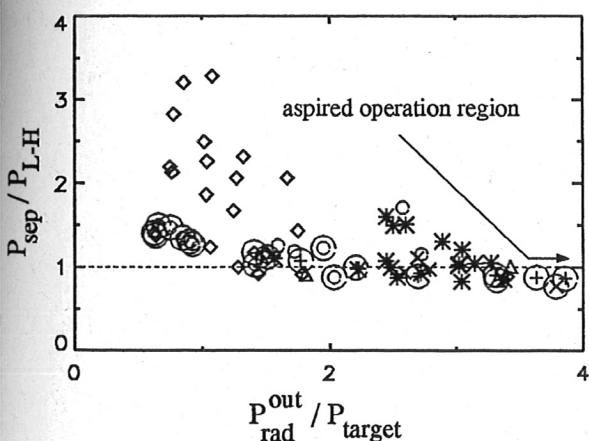


Figure 11: Power flux through the separatrix normalized to the L-H threshold power according to Eq. 1 versus the ratio of power radiated outside the separatrix and the target plate power load from thermography. The aspired operation point for a reactor would be the highest possible H-mode value of P_{out}^{rad}/P_{target} close to the $P_{sep}/P_{L-H} = 1$ line. Symbols marked by circles correspond to hydrogen plasmas with H^0 injection (high H-L threshold).

Important parameters for the performance of radiative discharges are the relative magnitudes of radiated power inside and outside the separatrix and the relation of the remaining power flow across the separatrix versus the H→L transition power flux. Fig. 10 shows P_{rad}^{in} and P_{rad}^{out} normalized by the total heating power versus the total target power load (in+out), P_{target} , from thermography, also normalized by P_{heat} . It is clearly seen, that the target power load reduction is obtained predominantly from radiation inside the separatrix. The ratio of radiation outside the separatrix and the target power load is shown in Fig. 11 versus the separatrix power flux

3.3 for low-threshold H-mode conditions. Radiative L-modes in hydrogen reach slightly higher values up to 4. All data points with high P_{rad}^{out}/P_{target} are situated near the H-mode threshold, including the L-mode data.

It may be concluded from Figs. 10 and 11, that the development of divertor concepts with better impurity entrainment is highly desirable, since especially for reactor conditions with high H→L threshold, a high value of $P_{rad}^{out}/P_{rad}^{in}$ will be required simultaneously with a high level of the total radiated power.

6 Z_{eff}

While the H-mode threshold represents one upper limit for the radiation level in a reactor, other and probably more restricting limits are fuel dilution and confinement degradation by central bremsstrahlung losses. Both drawbacks can be expressed by the effective plasma charge, Z_{eff} . Line-averaged values Z_{eff} are obtained from chord-integrated measurements of bremsstrahlung in the line-free visible region ($\lambda = 536 \text{ nm}$) on two different viewing chords (bremsstrahlung arrays with high spatial resolution operated in the near infrared are usually disturbed by thermal radiation from hot carbon tiles under high-power conditions). A radial viewing line with a tangency radius $\rho_{pol}^{tang} \approx 0.5$ was routinely available. Average densities and electron temperatures and their proper weighting functions for the calculation of \bar{Z}_{eff} were calculated for a few typical discharges with full $n_e(r)$ and $T_e(r)$ profile information available and parametrized for the use of routinely available signals (DCN interferometer chords for \bar{n}_e , stored energy and \bar{n}_e for \bar{T}_e) to establish a broad Z_{eff} database covering all classes of electron density profile shapes observed on ASDEX Upgrade.

For a smaller number of more recent discharges, also a toroidal viewing line for bremsstrahlung measurements with a tangency radius $\rho_{pol}^{tang} \approx 0.2$ was available. It is important to note the average radius

$$\bar{\rho}_{pol} := \frac{\int_{sightline} n_e^2(\rho_{pol}) \cdot f(T_e(\rho_{pol})) \cdot \rho_{pol} ds}{\int_{sightline} n_e^2(\rho_{pol}) \cdot f(T_e(\rho_{pol})) ds}$$

of the \bar{Z}_{eff} measurement: For $\bar{Z}_{eff}^{<0.5}$ we obtain $\bar{\rho}_{pol} \approx 0.75$, and for $\bar{Z}_{eff}^{<0.2}$, $\bar{\rho}_{pol} \approx 0.6-0.45$, the latter value typical of peaked n_e profiles (CDH-mode). Typically, the local weighting function (STALLCOP and BILLMAN, 1974), $n_e^2(\rho_{pol}) \cdot f(T_e(\rho_{pol}))$, is flat over the plasma core, since the weak temperature dependence (less than square-root), in combination with the rather peaked T_e profiles about cancels the quadratic n_e dependence due to the flatter n_e profile shape.

Figure 12 shows $\bar{Z}_{eff}^{<0.5}$ for the database (see Figs. 9 and 10) versus the main plasma radiation normalized by \bar{n}_e (this normalization is arbitrarily chosen for clarity because, at given Z_{eff} ,

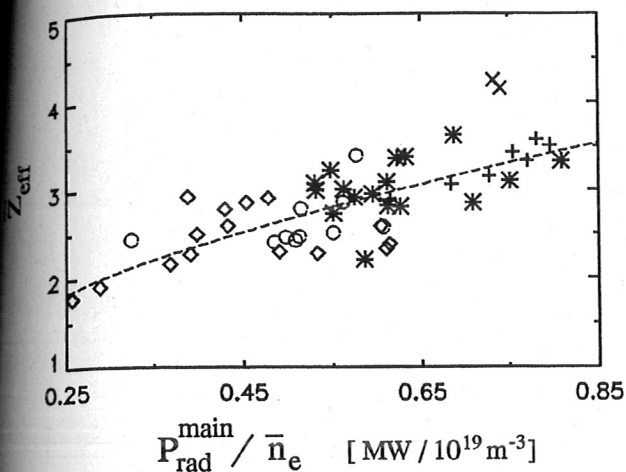


Figure 12: Line-averaged Z_{eff} (radial view, $\rho_{tang} = 0.5$) from bremsstrahlung measurements in the visible region ($\lambda = 536 \text{ nm}$) versus the radiated power in the main chamber normalized by the central line-averaged electron density. $P_{heat} = 7.4 \pm 0.5 \text{ MW}$. Average values of \bar{n}_e and P_{rad}^{main} of the data ensemble are $9 \cdot 10^{19} \text{ m}^{-3}$ and 5.1 MW , respectively. Symbols corresponding to Fig. 9.

the radiation is expected to rise stronger than linearly with \bar{n}_e (TOKAR, 1994)). A typical value for the CDH-mode is $\bar{Z}_{eff}^{\rho < 0.5} = 3$, with about equal contributions δZ_{eff} from intrinsic impurities (carbon dominated) and from the additional seed element (Ne, Ar or N). Generally, a rise in \bar{Z}_{eff} (or the corresponding increase in edge radiation) causes an increasing peaking of the electron density profile both in L and in H-mode, as shown in Fig. 13 (see also (BECKER, 1996)).

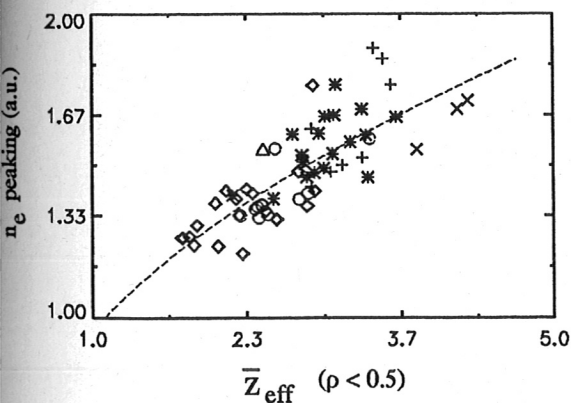


Figure 13: Peaking of the electron density profiles, obtained by the ratio of two DCN interferometer chords, versus line-averaged Z_{eff} (radial view, $\rho_{tang} = 0.5$).

Peaking factors for the Z_{eff} profiles are determined for a few discharges with the tangential bremsstrahlung measurement also available. Variations up to $\pm 20 \%$ are observed for the ratio of the central- versus the edge-weighted \bar{Z}_{eff} values, CDH-modes indicating central Z_{eff} peaking and radiative L-modes exhibiting hollow Z_{eff} profiles. Simulations with assumed Z_{eff} profile shapes suggest central values $Z_{eff}(0)$ up to 4 for the CDH-mode. A similar result is obtained from impurity transport calculations modelling the soft X-ray emission (DUX *et al.*,

sawtooth activity, which on the other hand only happens in the CDH mode (considering only high heating power scenarios).

7 Conclusions

Radiative scenarios with various impurities and plasma conditions have been investigated and compared for their performance in ASDEX Upgrade. Stationary CDH-modes are routinely obtained with neon injection exhibiting complete divertor detachment in the presence of high heating powers. In comparison to neon, argon shows higher radiation levels inside the separatrix and less SOL and divertor radiation. Owing to the stronger n_e peaking, it is unclear whether impurity accumulation in the center can be avoided and stationary CDH-modes can be achieved for ASDEX Upgrade conditions with argon. Nitrogen exhibits the most favourable values of the parameter $P_{rad}^{out}/P_{rad}^{in}$, however, up to now no 'quiescent' CDH-mode could be obtained due to the disturbing appearance of large compound-ELMs and early H \rightarrow L backtransitions. The values of $\bar{Z}_{eff} \approx 3$ and the even higher values on axis indicated by the central-tangential bremsstrahlung chord in the CDH-mode would be intolerably high in a reactor.

While there exists on ASDEX Upgrade a general trend of the electron density profile to peak with rising Z_{eff} , the peaking of Z_{eff} itself seems to occur exclusively in line with sawtooth suppression. Since n_e peaking may be welcome for the desired high-density reactor operation, the Z_{eff} peaking seen in the CDH-mode would be highly unwanted. Future experiments will have to show whether such peaking is avoided if sawtooth activity can be preserved during the CDH-mode, e. g., by central ICRF heating.

Recent experiments with neon and nitrogen seeding with the new JET Mark I divertor (THE JET TEAM, PRESENTED BY G. F. MATTHEWS, 1995) showed similar, high values of Z_{eff} , but in contrast to ASDEX Upgrade no peaking of the electron density profile and no confinement improvement (and also no Z_{eff} peaking) were observed during the radiative type-III ELM phase. It may be speculated that the property of the n_e profile to peak with rising Z_{eff} depends on the machine size, and therefore may be negligible for a reactor.

For the experimental parameter space covered in ASDEX Upgrade so far, high total radiation levels are always connected with only moderate radiation levels in the SOL and divertor. If this behaviour cannot be overcome by improved divertor concepts in the future, reduced target plate power load in a reactor can only be achieved under radiative H-mode conditions if $P_{sep}^{L \rightarrow H}$ is low. Better compression of impurities in the divertor is required to achieve higher divertor radiation levels along with a low impurity level in the main plasma. Discharges with high neutral pressure in ASDEX Upgrade tend to produce sufficient impurity compression, but

some energy confinement is sacrificed due to the high deuterium flux escaping to the main plasma.

The power flux into the separatrix, derived from the total heating power and deconvolution of bolometer measurements, was found to be indeed a good parameter to characterise the H-mode behaviour. Analysis of impurity-induced L-H-L transitions reveals that the L-H-L hysteresis is lost in radiative scenarios with high divertor neutral gas pressure. The usually lower H→L threshold is increased and matches the higher L→H threshold which does not deviate significantly from its standard value. The isotope effect, leading to about a factor of 2 higher threshold values in hydrogen plasmas is maintained, as well as the higher L→H threshold with ion ∇B drift away from the X-point. The loss of the L-H-L hysteresis comes along with an overall alignment of edge profiles and global energy confinement for radiative H- and L-modes, i.e. the usual bifurcation character of energy confinement between L and H mode is also lost eventually leading to a general convergence of H- and L-mode for highly radiative/gas puff conditions. Improved confinement observed in TEXTOR with high electron density and radiation levels (MESSIAEN *et al.*, 1994) is another hint for the at least partial alignment of (improved) L- and H-modes.

The rise of the H→L transition threshold is of major concern for ITER, since it may inhibit the anticipated high-density H-mode operation combined with radiative cooling. Another point of apprehension is the high value of Z_{eff} necessary in ASDEX Upgrade (and also JET) to obtain complete detachment which strongly exceeds the present limit anticipated for ITER ($Z_{eff} \leq 1.6$ (ITER-JCT AND HOME TEAMS, 1995)). Both findings may suggest to relax the maximum power flow limit in the ITER divertor to allow for, e.g., type-III ELMs burning through and fully attaching to the target plate. The radiative H-mode in a hydrogen plasma can act as a simulation for such a scenario, since its higher P_{sep}/P_{heat} value perhaps better matches the corresponding reactor conditions. However, the occurrence of strong compound ELMs typical for hydrogen discharges near the H→L threshold in ASDEX Upgrade, the origin of which is not understood so far, will have to be safely avoided in a reactor.

As the final conclusion, the observed behaviour of radiative discharges with high heating power demonstrates the necessity to develop more closed divertor arrangements with higher retention of hydrogen and impurities. This could result in a higher divertor radiation level for a given core contamination, at least a partial regain of the L/H hysteresis allowing H-mode operation at lower P_{sep} and possibly the achievement of larger H-factors which are usually observed at low main chamber neutral densities.

References

- ALLEN, S. L., BOZEK, A. S., BROOKS, N. H., *et al.* (1995). *Plasma Phys. Controlled Fusion* **37**, A191-A202.
- BECKER, G. (1996). *submitted to Nuclear Fusion*.
- BOSCH, H.-S., DUX, R., HAAS, G., KALLENBACH, A., KAUFMANN, M., MERTENS, V., MURMANN, H.-D., POSCHENRIEDER, W., SALZMANN, H., SCHWEINZER, J., SUTTROP, W., WEINLICH, M., ASDEX UPGRADE TEAM, and TEAM, N. (1996a). Invariance of Divertor Retention against External Particle Flow in Detached ASDEX Upgrade Discharges. accepted for publication in *Phys. Rev. Lett.*
- BOSCH, H.-S., GRUBER, O., HAAS, G., KALLENBACH, A., KAUFMANN, M., LACKNER, K., MERTENS, V., NEU, R., NEUHAUSER, J., RYTER, F., SCHWEINZER, J., ZOHM, H., ASDEX UPGRADE-TEAM, and NI-TEAM (1996b). accepted for publication in *Plasma Physics and Controlled Fusion*.
- DOYLE, E. J., GROEBNER, R. J., BURRELL, K. H., GOHIL, P., *et al.* (1991). *Phys. Fluids B* **3**, 2300-2307.
- DUX, R., KALLENBACH, A., BOSCH, H.-S., *et al.* (1996). 'Measurement and modelling of neon radiation profiles in radiating boundary discharges in ASDEX Upgrade', *submitted to Plasma Physics and Controlled Fusion*.
- FUCHS, J. C., MAST, K. F., HERRMANN, A., LACKNER, K., and ASDEX-UPGRADE, NI AND ICRH-TEAMS (1994). in *Controlled Fusion and Plasma Physics, Proc. 21st European Conference, Montpellier, 1994, European Physical Society, Geneva, Vol. 18 B, Part III*, 1308-1311.
- GRUBER, O., KALLENBACH, A., KAUFMANN, M., *et al.* (1995). *Phys. Rev. Lett.* **74**, 4217-4220.
- HAAS, G., BOSCH, H.-S., KALLENBACH, A., MEISEL, D., POSCHENRIEDER, W., ASDEX UPGRADE TEAM, and NBI TEAM (1995). Particle Exhaust and Wall Pumping Studies in ASDEX Upgrade. In KEEN, B., STOTT, P., and WINTER, J., editors, *Europhysics Conference Abstracts (Proc. of the 22th EPS Conference on Controlled Fusion and Plasma Physics, Bournemouth, 1995)*, volume 19C, part I, pages 321-324, Geneva. EPS.
- HERRMANN, W. and THE ASDEX UPGRADE TEAM (1995). *Phys. Rev. Lett.* **75**, 4401-4403.

- ITER-JCT AND HOME TEAMS (1995). *Plasma Phys. Controlled Fusion* **37**, A19-A35.
- KALLENBACH, A., DUX, R., MERTENS, V., *et al.* (1995). *Nucl. Fusion* **35**, 1231-1246.
- MESSIAEN, A. M., ONGENA, J., SAMM, U., *et al.* (1994). *Nucl. Fusion* **34**, 825-836.
- NEUHAUSER, J. *et al.* (1995). *Plasma Phys. Controlled Fusion* **37**, A37-A49.
- POST, D., ABDALLAH, J., CLARK, R. E. H., and PUTVINSKAYA, N. (1995). *Phys. Plasmas* **2**, 2328-2336.
- RAUPP, G., GRUBER, O., KALLENBACH, A., MERTENS, V., NEU, G., TREUTTERER, W., ZEHETBAUER, T., ZASCHE, D., and THE ASDEX UPGRADE TEAM (1995). 'Discharge Supervision Control on ASDEX Upgrade', submitted to *Fusion Technology*.
- RYTER, F., ALEXANDER, M., FUCHS, J. C., GRUBER, O., KALLENBACH, A., *et al.* (1994a). in *Controlled Fusion and Plasma Physics, Proc. 21st European Conference, Montpellier, 1994, European Physical Society, Geneva, Vol. 18 B, Part I*, 330-333.
- RYTER, F., BÜCHL, K., FUCHS, C., GEHRE, O., GRUBER, O., *et al.* (1994b). *Plasma Phys. Controlled Fusion* **36**, A99-A104.
- SAMM, U., BERTSCHINGER, G., BOGEN, P., HEY, J. D., HINTZ, E., KÖNEN, L., LIE, Y. T., POSPIESZCZYK, A., SCHORN, R. P., SCHWEER, B., TOKAR, M., and UNTERBERG, B. (1993). *Plasma Phys. Controlled Fusion* **35**, B167-B175.
- SHAING, K. C. and HSU, C. T. (1995). *Phys. Plasmas* **2**, 1801-1803.
- STALLCOP, J. R. and BILLMAN, K. W. (1974). *Plasma Physics* **16**, 1187-1189.
- THE JET TEAM, PRESENTED BY G. F. MATTHEWS (1995). *Plasma Phys. Controlled Fusion* **37**, A227-A239.
- TOKAR, M. Z. (1994). *Nucl. Fusion* **34**, 853-861.
- ZOHM, H., OSBORNE, T. H., BURRELL, K. H., *et al.* (1995). *Nucl. Fusion* **35**, 543-550.